applied nano

MDPI

Article

Tailoring Piezoresistive Performance in 3D-Printed Nanocomposite Sensors Through Cellular Geometries

Md Ibrahim Khalil Tanim and Anahita Emami *

Ingram School of Engineering, Texas State University, San Marcos, TX 78666, USA; gwu6@txstate.edu
* Correspondence: a.emami@txstate.edu

Abstract: Flexible nanocomposite sensors hold significant promise in various applications, such as wearable electronics and medical devices. This research aims to tailor the flexibility and sensitivity of 3D-printed piezoresistive nanocomposite pressure sensors through geometric design, by exploring various simple cellular structures. The geometric designs were specifically selected to be 3D printable with a flexible material, allowing evaluation of the impact of different structures on sensor performance. In this study, we used both experimental and finite element (FE) methods to investigate the effect of geometric design on piezoresistive sensors. We fabricated the sensors using a flexible resin mixed with conductive nanoparticles via a Stereolithography (SLA) additive manufacturing technique. Electromechanical testing was carried out to evaluate the performance of four different sensor designs. Finite element (FE) models were developed, and their results were compared with experimental data to validate the simulations. The results demonstrated that auxetic structure exhibited the highest sensitivity and lowest stiffness both in experimental and FE analysis, highlighting its potential for applications requiring highly responsive materials. The validated FE model was further used for a parametric study of one of the promising simple designs, revealing that variations in geometric parameters significantly impact piezoresistive sensitivity. These findings provide valuable insights for advancing the development of pressure sensors with tailored sensitivity characteristics.

Keywords: additive manufacturing; flexible pressure sensors; cellular structures; piezoresistivity; polymer nanocomposite

Citation: Tanim, M.I.K.; Emami, A. Tailoring Piezoresistive Performance in 3D-Printed Nanocomposite Sensors Through Cellular Geometries. *Appl. Nano* **2024**, *5*, 258–278. https://doi.org/10.3390/applnano5040017

Academic Editor: Angelo Maria Taglietti

Received: 21 September 2024
Revised: 22 November 2024
Accepted: 22 November 2024
Published: 26 November 2024

1. Introduction

Polymer nanocomposites are widely recognized for combining the advantageous properties of polymers and nanomaterials. By incorporating nanoparticles such as silver nanowires, graphene, carbon nanotubes, and metal nanoparticles into a polymer matrix, these composites achieve performance levels that surpass those of the individual components [1–3]. The high surface area of nanoparticles relative to their volume contributes to enhanced properties like electrical conductivity, thermal stability, and mechanical strength. In addition to these traditional improvements, polymer nanocomposites exhibit distinctive functionalities, such as piezoresistivity. This unique property allows the materials to alter their electrical resistance in response to mechanical strain, making them suitable for advanced applications in sensor technology [4–6] and smart materials [7].

Flexible polymer nanocomposite sensors are particularly notable for their integration of piezoresistive behavior with mechanical flexibility, which is ideal for applications requiring both flexibility and sensitivity, such as wearable technology [8–10] and health monitoring systems [11–14]. These sensors surpass conventional rigid sensors by offering improved sensitivity and stretchability, leading to better skin conformity and more accurate health data [15]. A recent study has explored hierarchical structures by replicating the lotus leaf, which significantly enhances both sensitivity and linearity in pressure sensors and addresses the challenges of saturation and nonlinear response under high pressure [16].

Unlike traditional healthcare devices, which often lack portability and wearability, electronic skin (E-skin) sensors excel at detecting subtle pressure changes and are well suited for personal health monitoring. Xuewen Wang et al. [11] developed a pressure sensor using microstructured PMDS thin film with high-quality silk as a mold, resulting in E-skins with rapid response times and notable durability. Haiyu et al. [17] developed an E-skin sensor that has a sensitivity of 4.4 kPa^{-1}, a response time under 10 ms, and a minimum detection limit of 0.5 Pa. It has the ability to withstand over 11,000 usage cycles. Their fabrication process is also noted for being cost-effective and time-efficient.

The growing use of flexible sensors in wearable electronics highlights their ability to be integrated into items like stockings and gloves or directly on the skin to monitor body signals effectively [18,19]. These sensors provide superior flexibility and stretchability compared to traditional wearables, making them essential for tracking real-time movements. For example, a flexible sensor developed using carbon nanotubes exhibited over 900% stretchability, rapid response, high sensitivity, and durability. A graphene-based flexible sensor, developed with stretchable yarns and polyvinyl alcohol (PVA), demonstrated high sensitivity and stretchability up to 150%, detecting both large human movements and subtle actions such as speaking and breathing [20].

Recent advancements in multifunctional sensors have focused on developing adaptable sensors that offer wide-ranging utility. Wang et al. [21] introduced a multifunctional sensor inspired by natural skin that detects compressive, bending, and twisting strains with high gauge factors and can sense humidity and pressure with a fast response time. Zhen Lou et al. [12] developed a pressure sensor combining P(VDF-TrFe) with conductive rGO, capable of monitoring physiological signals and detecting light forces. Additionally, the adoption of advanced piezoresistive materials like MXenes and multilayered graphene has led to the development of highly sensitive sensors, making them suitable for wearable applications [16]. Yu et al. [8] developed a flexible pressure sensor using polylactic acid (PLA) with tissue paper impregnated with porous MXene, providing high sensitivity, a large sensing range (up to 30 kPa), and durability. These sensors are ideal for biomonitoring, synthetic skins, and human–machine interfacing technologies. Zhang et al. [22] created a flexible nanocomposite sensor using a PVA hydrogel matrix incorporated with 2D Mxenes, which provide high sensitivity and strong adhesion. This is suitable for health monitoring systems because of the adhesion and self-healing properties. Because of the high sensitivity and rapid response times, flexible piezoresistive sensors are suitable for various biomedical applications like the detection of pressure fluctuation and sound variation. Wang et al. [13] developed miniaturized piezoresistive pressure sensors using poly(3,4-ethylenedioxythiophene): poly (styrene sulfonate) (PEDOT: PSS) composite films incorporated with graphene oxide (GO) on a flexible substrate.

The development of functional polymer nanocomposites with optimized piezoresistive response has largely focused on material-centric approaches. The approaches typically include the manipulation of nanoparticles' structures [23,24], concentrations [10], and polymer matrix morphologies [25–27]. Though these strategies have led to improvements in piezoresistive performance, they are often empirical, and because of the complex interactions within the material systems, they lack efficiency [27]. Therefore, there has been a need for a more universal and systematic methodology in materials engineering. Recent studies have explored sensor topology as a critical factor in enhancing performance. For example, Yun-An Lin et al. [28] developed a wearable strain sensor by integrating graphene-coated kinesiology tape (K-Tape) to create a highly sensitive and self-adhering sensor. The sensor enables detailed spatial strain sensing by exploring mesh topologies. The piezoresistive responses can also be varied using different structures such as serpentine, auxetic, and kirigami [29]. Long Wang et al. [27] presented a design methodology to manipulate the piezoresistive effect of nanocomposites and achieved varied strain sensitivities without altering the material system. Their study demonstrated that stress-concentrating topologies enhance strain sensitivity while stress-releasing topologies significantly suppress bulk film piezoresistivity. Similarly, the sensitivity of the flexible pressure sensors can be tailored

by adjusting the infill patterns during additive manufacturing. James Bank et al. [30] used common infill patterns that showed notable variations in sensitivities under varying pressure conditions.

Despite these advances, the potential of topological design to enhance piezoresistive performance is still not well understood. Recognizing the gap, this study investigates how different topological configurations can affect the piezoresistive sensitivity of flexible pressure sensors without altering the material system. First, we fabricated piezoresistive composite pressure sensors with four 3D printable topological configurations, namely square, diamond, ellipse, and auxetic. These topologies were subjected to electromechanical testing to characterize the piezoresistive sensitivity. Second, the experimental data collected were used to determine the material properties in finite element analysis (FEA) and then compared with the results from the experiments to validate the FEA model. Last, a parametric study was conducted on the ellipse structure using the validated FEA model. The parametric study enabled us to systematically investigate the influence of different design parameters of a single structure on piezoresistive sensitivity. This comprehensive analysis not only supported our experimental findings but also provided more profound insights into how topological variations can be strategically used to enhance sensor performance.

2. Theoretical Background

2.1. Cellular Structure for Additive Manufacturing Subsection

Cellular structural design has a significant impact on additive manufacturing (AM) in engineering applications. The advent of additive manufacturing has extended the possibilities for designing cellular materials beyond the traditional forms and enabled greater design freedom. However, it has also introduced new complexities in decision-making to achieve the optimal design. Several factors should be considered to bring out the optimal design for specific applications, such as the best unit cells, optimal cell parameters, integration of cells with larger forms, etc.

Cellular solids can be classified [31] into four types: honeycomb, open-cell foam, closed-cell foam, and lattice structures. The classification of cellular solids is important for selecting appropriate structures for specific applications.

These types of structures have geometrical features or discontinuities that cause increased stress in a localized area. The degree of stress concentration is measured by the stress concentration factor (Kt) [32]. The application of stress leads to a change in the material's electrical properties (resistance) in piezoresistive pressure sensors. As the piezoresistive material has conductive nanoparticles, the localized conductive region gets affected by compression or tensile forces. For example, when the material is subjected to tensile forces, the distance between individual nanoparticles or their groups increases because of the deformation in the structure. Thus, the number of inter-nanoparticle connections decreases, and this phenomenon reduces the conductive pathways for electricity inside the composite [27]. As a result, there is an increase in the electrical resistance of the overall structure.

2.2. Piezoresistivity

Polymers are typically poor electrical conductors due to the lack of free electrons. However, when conductive nanofillers are added to the polymer matrix, the composite materials become suitable for piezoresistive applications. The application of compressive force to the matrix causes the nanoparticles to move closer to each other as shown in Figure 1.

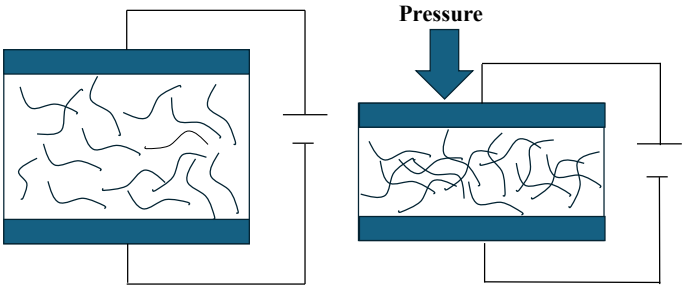

Figure 1. Conductive pathways are generated upon compression.

When the concentration of these nanoparticles reaches a certain threshold, they form an interconnected network spanning the entire material. This network allows electrons to flow through the composite, which reduces its resistivity and enhances its electrical conductivity significantly. Piezoresistivity refers to the relationship between the force applied to a material and the resulting change in its resistance. This correlation is defined by a specific relationship that connects the material's strain to its resistance change. For pressure sensors, the pressure sensitivity S can be written in terms of resistance R and stress σ.

$$\frac{\left(\frac{|R-R_0|}{R_0}\right)}{\sigma} = \frac{\frac{\Delta R}{R_0}}{\sigma} = S \tag{1}$$

The pressure sensitivity S can be written in terms of voltage and stress σ.

$$\frac{\left(\frac{|V-V_0|}{V_0}\right)}{\sigma} = \frac{\frac{\Delta V}{V_0}}{\sigma} = S \tag{2}$$

3. Experimental Section

3.1. Material Selection

The development of flexible sensors requires meticulously balancing the properties of various materials. These materials are classified into metallic, carbon-based, and polymer materials [15].

Metals are frequently used for their high conductivity and versatility. The common choices include copper, silver, zinc, and gold, which are often used in films, nanowires, and nanoparticles [33]. One of the most utilized materials is silver nanowires. They offer excellent conductivity and antibacterial properties but are prone to entanglement under stress, which reduces sensitivity. Copper nanowires are more affordable, but they oxidize easily [34]. Gold nanowires are more stable but expensive [35]. Liquid metals like Eutectic Gallium Indium (EGaIn) have shown promise in biomedical applications because of their biocompatibility and flexibility, but the handling challenges remain [36]. Metal oxides such as zinc oxide (ZnO) nanowires enhance durability and sensitivity [37]. Lee et al. [38] developed a strain sensor with zinc oxide nanowires, which demonstrated that the gauge factors reached 7.64 when combined with reduced graphene oxide (RGO).

Carbon-based materials such as carbon black, carbon nanotubes (CNTs), and graphene are commonly used in flexible pressure sensors. As these materials provide excellent conductivity and adaptability, they are mixed with polymer matrices for the fabrication of sensors. Carbon black is an economical choice that enhances the conductivity and stretchability of the composite [39]. Carbon nanotubes (CNTs) are frequently used for pressure sensor applications. The single wall CNTs offer higher sensitivity and uniformity than multi-walled CNTs but face durability issues over extended use [40]. Graphene has a high aspect ratio and good conductivity, making it an exceptional choice for piezoresistive sensors [41,42].

Polymers are used as matrix materials to manufacture the sensors. Polydimethylsiloxane (PDMS), polyurethane (PU), polyimide, etc., are the most common flexible polymers.

They are often combined with conductive fillers like graphene or metallic nanoparticles to achieve the piezoresistive effect. For example, poly-methyl methacrylate (PMMA) integrated with graphene creates sensors with high sensitivity and durability [42]. However, ensuring homogeneous dispersion of fillers in the polymer matrix is crucial to prevent inconsistencies in performance.

The materials used in this study include photopolymer flexible resin (3Dresyn TFA70) [43] and conductive graphene nanoparticles [44]. Graphene has been used due to its exceptional electrical and mechanical properties. As one of the thinnest materials known, it demonstrates a linear change in resistance with strain, making it an excellent candidate for piezoresistive sensor applications [42,45–47]. The properties of materials used in this study are listed in Table 1.

Table 1. Properties of materials.

Properties of TFA70 [43]	Properties of Graphene Nanoparticles [32]
• Tensile strength < 10 MPa • Flexural strength < 10 MPa • Soft and elastic (Young modulus < 10 MPa) • Elongation > 50%	• Lateral sizes are approximately 100 nm • Sheet resistance > 150 kΩ/square • Resistivity > 40 Ω.m • Conductivity < 30 mS/m

3.2. Design of Sensors

Four different structures, along with a reference sample, were designed using SolidWorks 2024, as shown in Figure 2, and fabricated through SLA additive manufacturing techniques. Each structure measures 10.5 mm in height, width, and depth. The selection of these cellular structures was based on their distinct mechanical behaviors. For instance, the structure with square holes was chosen for its load-bearing capability. The stress concentrates around the edges of the holes and leads to localized buckling or bending under load conditions [48]. This stress concentration can cause significant changes in resistance in piezoresistive material [27]. The diamond (rhombus) lattice structure is studied for its mechanical properties like elastic modulus and critical buckling load [49]. This structure is also known for its self-supporting properties [49]. The elliptical structure was chosen due to its absence of sharp edges or corners, which affects stress concentration differently compared to the diamond holes. The auxetic structure has unique mechanical properties like having a negative Poisson's ratio [50] which offers high flexibility and a reduced propensity to buckle compared to conventional cellular structures.

3.3. Fabrication of Sensors

The SLA 3D printer used in this study was Anycubic Photon D2. The digital light projection (DLP) technique was used in this 3D printer, and UV-LED base light sources provided the wavelength at 405 nm. The photopolymer resin was heated to 40 °C to reduce the viscosity. This increased the flowability and made the resin easier to mix with nanoparticles. Conductive nanoparticles were incorporated into the flexible resin for the 3D printing of piezoresistive material. The optimum quantity of conductive nanoparticles in composite resin is important for forming a continuous conductive path and preventing nanoparticle agglomeration. The resin was mixed with 2%wt graphene nanoparticles, and the mixture was placed in a vortex mixer to ensure an even distribution of the nanoparticles. The sample containing 2%wt of graphene, as recommended by 3Dresyn [44], showed a significantly low resistance range, measuring below 0.5 MΩ.

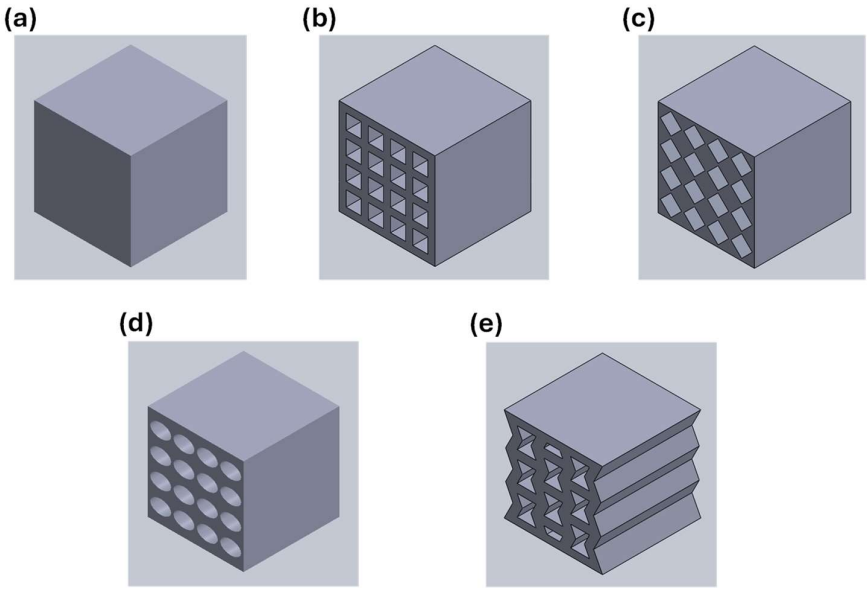

Figure 2. (**a**) Reference sample, (**b**) square structure, (**c**) diamond structure, (**d**) elliptical structure, (**e**) auxetic structure.

The mixture was sonicated in an ultrasonic bath to break down any nanoparticle agglomerates and disperse them uniformly in the resin, resulting in a more homogenous mixture. The mixtures were brought into a vacuum chamber to remove trapped air bubbles that could cause defects in the final product. Degassing is crucial for ensuring the mechanical strength and integrity of the material. The prepared resin was further warmed before printing. Printing parameters play key roles in SLA additive manufacturing because unoptimized printing parameters affect the printed parts' quality, accuracy, and mechanical properties. These parameters include layer thickness, build-plate lift speed, and curing time (Figure S1). The print speed can vary depending on the layer thickness. Thicker layers can reduce print time but lower quality, while thinner layers ensure quality but increase print time. The lift speed of the build plate significantly affects the printing of flexible materials. A slower lift speed allows for adequate bonding time, thus improving layer adhesion. It also allows the material to settle into the desired shape, ensuring accuracy and precision. Lowering lift speed reduces the peeling force, which prevents damage to the flexible resins when detaching from the FEP film. Thus, the lift speed is crucial for preserving the structural integrity and dimensional accuracy of printed objects. Figure 3 shows the flowchart of the manufacturing process.

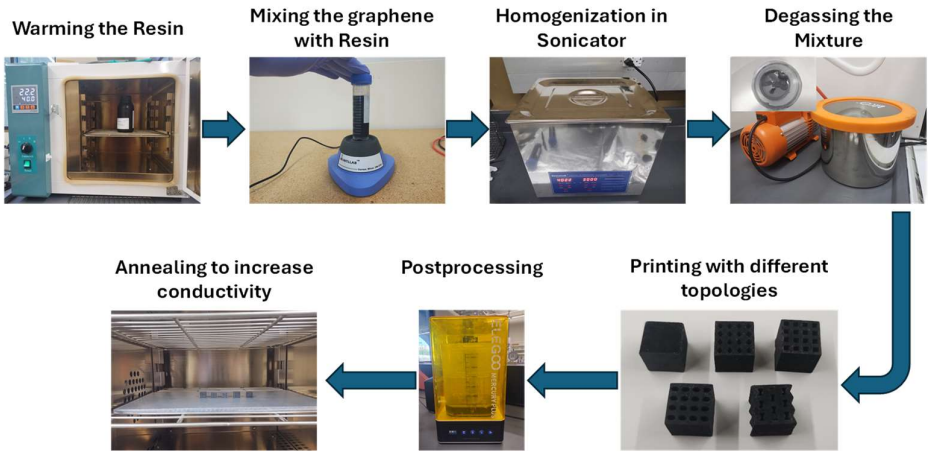

Figure 3. Flowchart of the manufacturing process.

The curing time determines how long the resin is exposed to the light source to be cured. A shorter curing time can reduce the printing time but might lead to under-cured parts, which can affect the mechanical properties and accuracy. On the other hand, longer curing times bring out better quality but increase the printing time. Thus, finding the optimum curing time is necessary to achieve optimal printed part quality. As the nanoparticle blocks the UV light, the curing time is much longer than that of the neat resin. Table 2 shows the optimum printing parameters used in this study for the flexible neat resin.

Table 2. Printing parameters for composite resin.

Printing Layers	Layer Thickness (mm)	Curing Time (s)	Build Plate Lift Speed (mm/min)
Bottom layers	0.05	90	120
Normal layers	0.05	40	60

The printing process was followed by postprocessing, which included cleaning of uncured resin and post-curing. Post-curing involved additional exposure to UV light to ensure complete curing and optimal material properties.

The cellular structures were designed to maintain a consistent void fraction of 28.44% so that the topological variations only affect the results. There were slight variations in the weight in the SLA 3D-printed samples. The weights of these printed cellular structures were measured to range from 0.90 g to 0.92 g. This variation can be attributed to the resolution of the 3D printer. Higher resolution results in greater printing accuracy.

Finally, the printed structures were annealed at 100 °C for 20 min in an oven. This process can help to increase the electrical conductivity of the composite structures. Annealing reduces defects and residual stresses [51] within the material, which results in a more stable and uniform structure. It also increases the degree of crystallinity in the polymer matrix [52], which leads to better alignment of polymer chains and improved charge carrier pathways. In addition, annealing improves the distribution and networking of conductive fillers, creating continuous conductive pathways [53]. This thermal treatment also enhances interfacial adhesion [54] and reduces the resistance between the polymer matrix and conductive nanoparticles. The resistance of the reference sample was measured before and after the annealing process and was found to have decreased by 10–20% through the two-point probe method.

3.4. Electromechanical Testing Setup

When piezoresistive materials are compressed, there is a change in the resistance as the distances between the conductive nanoparticles change. A specialized experimental setup is necessary to measure the resistance of piezoresistive material under compression. In Figure 4, an overview of the experimental setup is demonstrated.

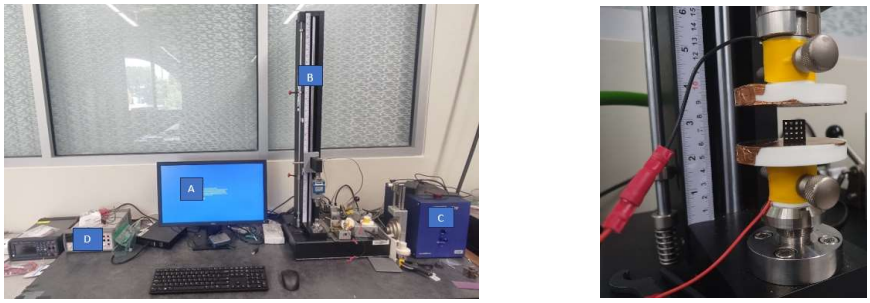

Figure 4. Overview of experimental setup.

The control computer with NI LabVIEW 2021 and MTTESTQuattro (version 7.01.04) software is labeled as A in the figure. The ADMET Universal Testing Machine (UTM) used

to obtain the experimental results is labeled as B, the UTM control box is labeled as C, and the digital multimeter (DMM) is labeled as D.

The compression platens were wrapped with copper film to measure the change in conductivity during the compression test. Copper films were used due to their high conductivity. These copper films were connected with DMM to measure the change in resistance of the test sample.

The UTM sends an analog voltage on a scale from 0–10V corresponding to the maximum force and maximum position in MttestQuattro (version 7.01.04) software which are defined by the user.

For multimeter options in NI LabVIEW 2021 software, the maximum resistance is self-explanatory. This is the highest resistance one expects to measure. The sample rate is dependent upon the integration time of the DMM. While faster sample rates can improve data resolution, they may also introduce more noise and reduce measurement precision. The accuracy of measurements can be influenced by the displacement rate and the DMM's capability to handle high-frequency data.

4. Finite Element Analysis

4.1. Material Model

The Mooney–Rivlin and Yeoh models are widely used hyperelastic material models for finite element analysis. Both are constitutive models for rubber-like materials suitable for large-strain elastic problems. The Mooney–Rivlin model for incompressible materials is defined by a strain energy density function, which is described by the following equation [55]:

$$U = C_{10}(\bar{I}_1 - 3) + C_{01}(\bar{I}_2 - 3) \tag{3}$$

where U is strain energy density, $\bar{I}_1$ and $\bar{I}_2$ are the first and second strain invariants, and C_{10} and C_{01} are empirical material parameters. The Yeoh model for incompressible materials expands the Mooney–Rivlin model by incorporating a quadratic term to address nonlinear effects [56]. The following equation represents this model and can be used to better capture the material behavior under large deformations.

$$U = C_{10}(\bar{I}_1 - 3) + C_{20}(\bar{I}_1 - 3)^2 + C_{30}(\bar{I}_1 - 3)^3 \tag{4}$$

where C_{10}, C_{20}, and C_{30} are empirical material parameters.

The relationship between resistivity and stress had been derived from empirical results obtained from the electromechanical testing of solid cubic materials. An empirical model was fitted to the experimental results and was used to define the electrical properties in the finite element model (FEM). Resistivity was modeled as a function of stress along the applied load using the USDFLD subroutine. As a result, any induced stress caused corresponding changes in resistivity. These properties were applied across the different samples to study the effect of cellular geometries on the piezorestivity of these sensors.

4.2. Boundary Condition

The test samples, which include four different topologies and a reference sample, were analyzed under a uniformly increasing pressure, ramping linearly from 0 to 30 kPa, applied to the top surface of a rectangular plate. The objective was to observe the potential difference at the top surface of the reference sample. Zero voltage was applied to the bottom surface, while a constant current was applied to the top surface of the sample. To prevent slippage, all rotational and translational movements of the bottom rectangular plate were restricted in all directions, whereas the top plate used for compression was directed only along the Y-axis (Figure S2). The compression plates were made of steel with Young's modulus of 210 GPa and a Poisson's ratio of 0.3, representing the rigid plates (relative to flexible samples) used for compressing the samples. Minor sliding in the contact area was accounted for with a coefficient of friction of 0.3.

4.3. Mesh

The FEA is based on the hybrid formulation of structural and electrical analysis. The mesh element type selected for this analysis is Q3D8H which is a hexagonal element type with eight nodes and compatible for hybrid analysis. As the results vary with mesh element size, the FEA is conducted using three different element sizes. Initially, analysis was performed on the cellular structures with an element's length size of 1.05 mm. Later, we refined the mesh by reducing the mesh element size to 0.53 mm to get better results. We determined the stress value with respect to mesh element size for each structure. For this comparison, we chose an analytical rigid body (Figure 5a) to compress the sample and a steel plate as a substrate. As the analytical rigid body has no material properties, it has no impact other than uniform compression. Then, we designed two steel plates: one for the substrate and another one for compression instead of the analytical rigid body (Figure 5b).

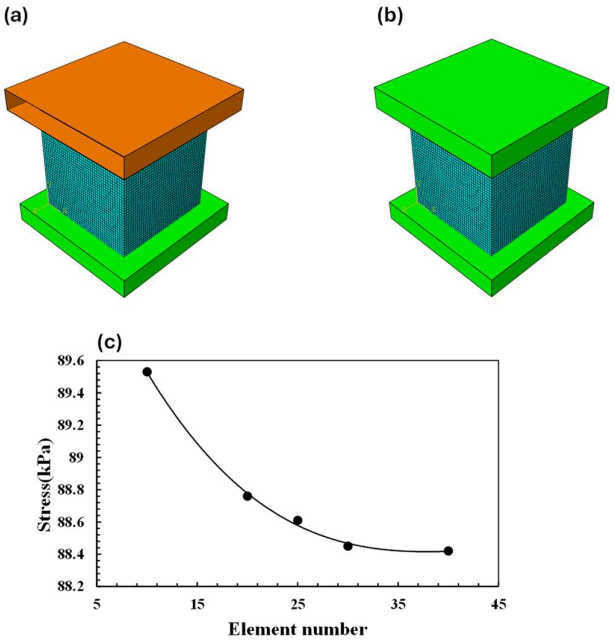

Figure 5. (**a**) Analytical rigid body for compression, (**b**) Steel plate for compression, (**c**) Mesh convergence graph for reference sample.

The stress value of the steel plate is comparatively higher due to its material properties. After that, we refined the mesh element size to investigate the stress values. The finer we refined the mesh the better results we got. In other words, the stress values converged as we increased the element number. Figure 5c demonstrates the stress values with respect to the number of elements for each topology.

5. Results and Discussion

5.1. Mechanical Behavior

5.1.1. Experimental Results

The stress and strain curves of the topologies (Figure 6) show the mechanical behavior of samples under compression. The sample with the highest stiffness is the reference sample, which has a solid cubic geometry with no porosity which represents the mechanical behavior of the nanocomposite material used in this study. The auxetic structure exhibits the highest flexibility for the given stress. The order of stiffness based on the experimental analysis is reference > diamond > square > ellipse > auxetic structure.

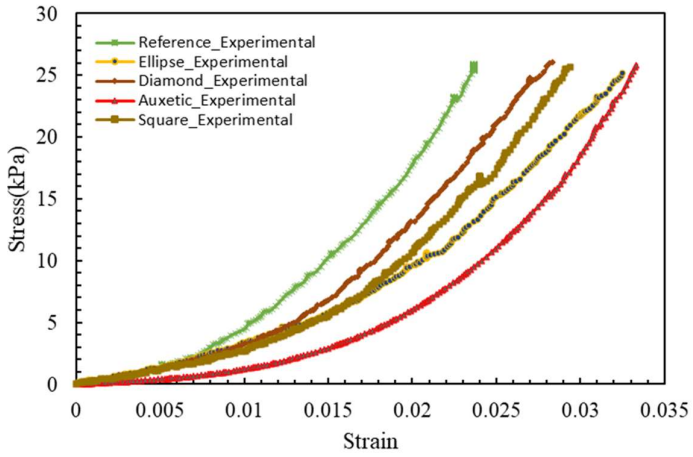

Figure 6. Experimental stress vs. strain curve of all topologies.

5.1.2. Finite Element Analysis Results

The mechanical behaviors of 3D-printed samples were analyzed by fitting the reference sample's experimental stress–strain data with two hyperelastic material models, the Mooney–Rivlin and Yeoh models. This evaluation aimed to compare their performance by assessing how well they fit the experimental data.

The experimental stress–strain data were analyzed using nonlinear regression techniques to fit both models and determine the best-fit parameters. The fitting process resulted in the following parameters: for the Mooney–Rivlin model, C10 = −0.0234 MPa and C01 = 44.44 MPa; for the Yeoh model, C10 = 0.0883 MPa, C20 = 29.60 MPa, and C30 = 443.21 MPa. Figure 7 presents the stress–strain curves for the Mooney–Rivlin and Yeoh models in comparison with the experimental results. The Mooney–Rivlin model failed to accurately capture the experimental data, indicating that the material's behavior is more complex than the model can represent. In contrast, the Yeoh model provided a good fit up to strain values exceeding 2%, due to the inclusion of the quadratic term and a cubic term, which address nonlinear effects. This comparison helps in selecting the material model that best captures the deformation behavior for a more accurate FEA using Abaqus (version 2023) software.

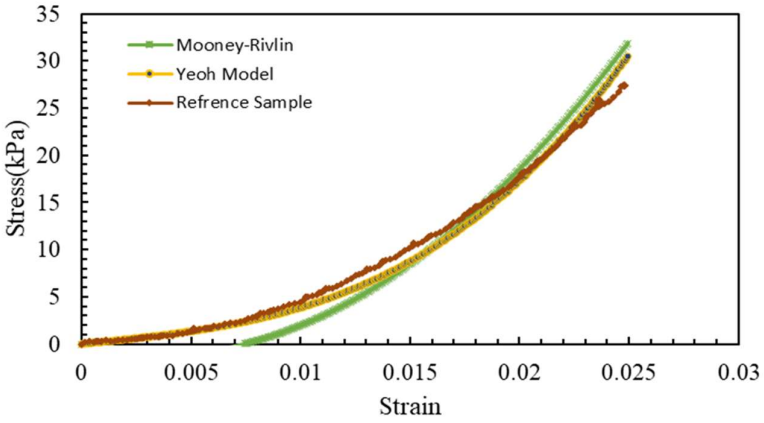

Figure 7. Hyperelastic material models.

Each structure was subjected to the same uniform pressure, and a finite element analysis was conducted to observe how the stress concentrates along the structures. Figure 8 demonstrates the localized stress concentration areas.

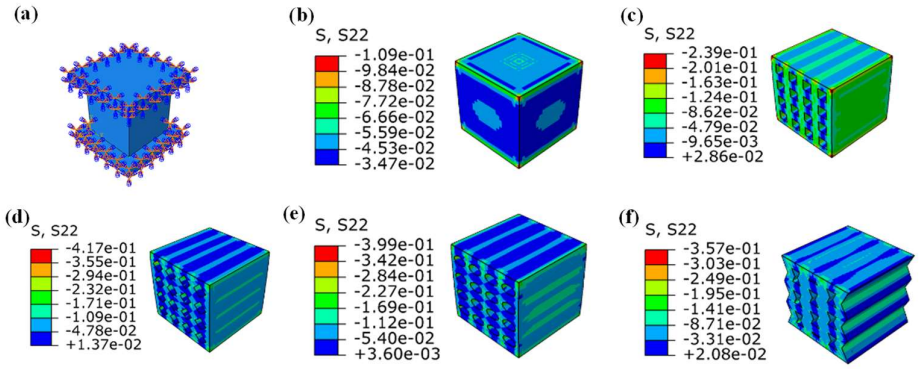

Figure 8. (**a**) FEA setup, stress concentration in FEA, (**b**) reference sample, (**c**) square structure, (**d**) diamond structure, (**e**) ellipse structure, (**f**) auxetic structure.

The porous sections experienced more stress concentration due to their reduced cross-section area. Pressure and engineering strain data were collected to compare the structural behavior. The node at the middle of the top surface was selected to measure the average displacement and strain in the pressure sensor. Figure 9 shows the stress–strain curve results obtained from FEA for different structures.

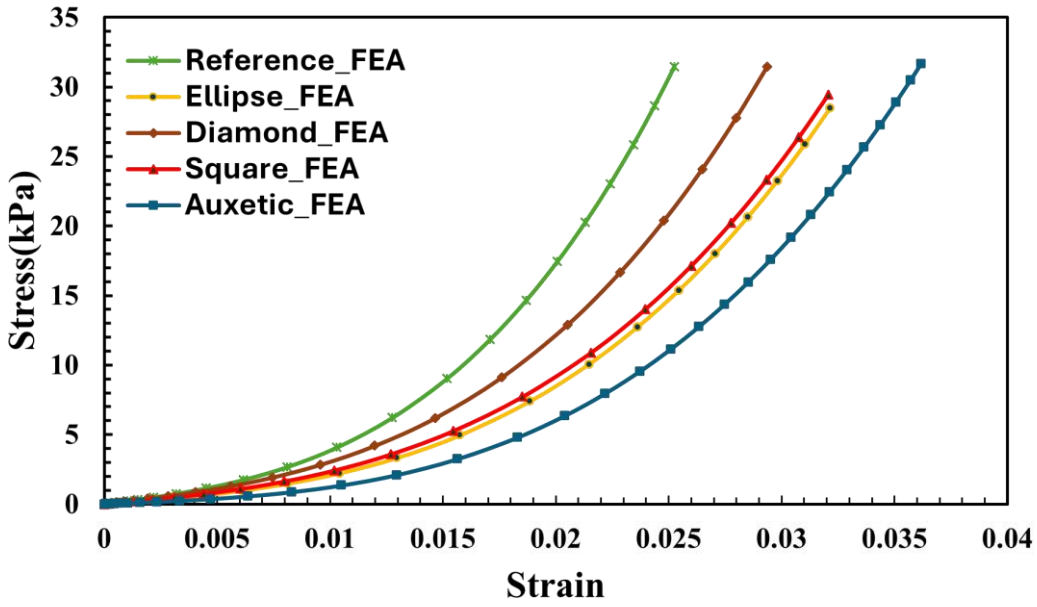

Figure 9. Finite element analysis results for all topologies.

Figure 10 shows the comparison between FEA and experimental results for different structures. These results validate the use of FEA in evaluating the mechanical behavior of various architectured samples for design optimization.

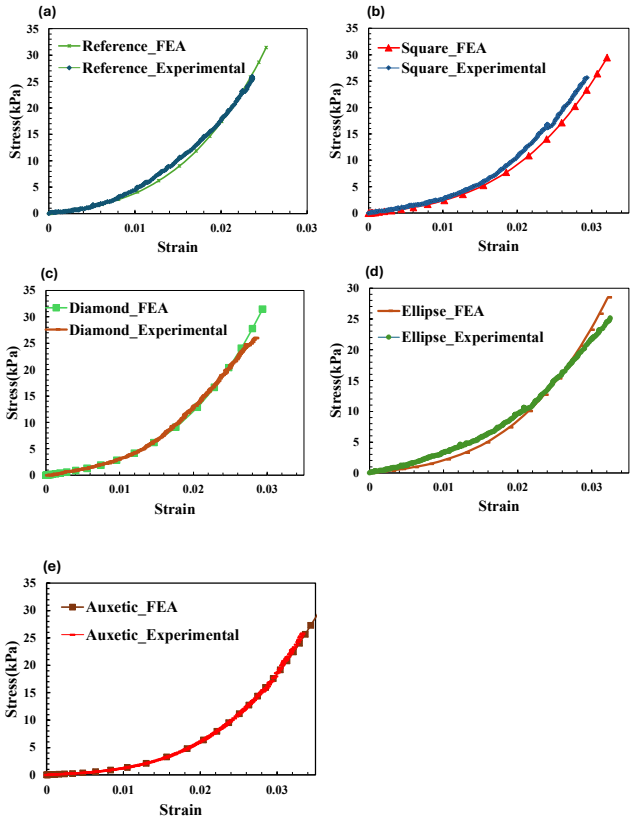

Figure 10. Stress vs. strain curves from experimental and FEA of (**a**) reference sample, (**b**) square structure, (**c**) diamond structure, (**d**) ellipse structure, (**e**) auxetic structure.

Minor discrepancies that can be observed, particularly in the square and ellipse structures, might be attributed to imperfections in the 3D-printed samples. These imperfections include trapped air bubbles that were not fully eliminated in the degassing steps during resin preparation for the 3D printing.

5.2. Electrical Behavior

5.2.1. Experimental Results

The composite piezoresistive structures showed significant sensitivity characteristics under different stress levels. Figure 11 illustrates the absolute value of normalized resistance change ($\Delta R/R_0$) as a function of stress for various topologies. A preload of 0.1 N was applied before initiating the electromechanical testing to establish adequate contact between the compression platens and the sensor, resulting in the initial offset observed in all the curves. This figure indicates that the composite structures had high sensitivity at very low pressures. The sensitivity can be divided into two distinct regions. The first region, up to 5 kPa, is marked by a steep curve for each topology, which indicates higher piezoresistive sensitivity. Figure 11a demonstrates these two sensitive regions, and the stress-free resistances are shown in Figure 11b. In the high-sensitive region, the order of sensitivity was auxetic > ellipse > square > diamond > reference sample. This ranking highlighted the superior performance of the auxetic structure, likely due to its unique geometric configuration that enhances deformation under stress.

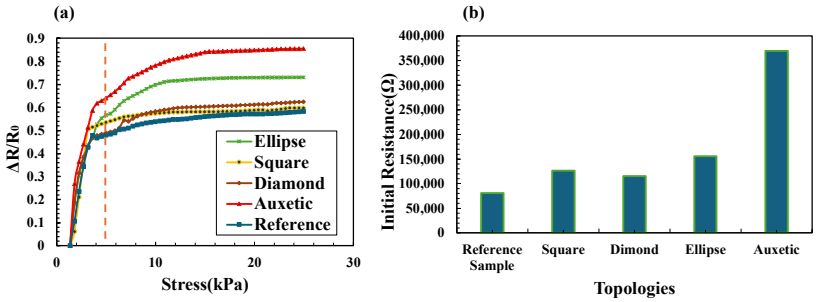

Figure 11. (**a**) $\Delta R/R_0$ vs. stress curves for each topology, (**b**) initial resistance.

As pressure increased beyond 5 KPa and went up to 25 KPa, the rate of change of resistance decreased, which indicated a lower sensitivity. The curves in this range were less steep, showing reduced responsiveness of the structures to stress. Figure 12 highlights the higher sensitivity region. The auxetic structure maintained the highest sensitivity in this range, while the ellipse structure also showed significant sensitivity. The square structure exhibited higher average sensitivity than the diamond structure in both regions.

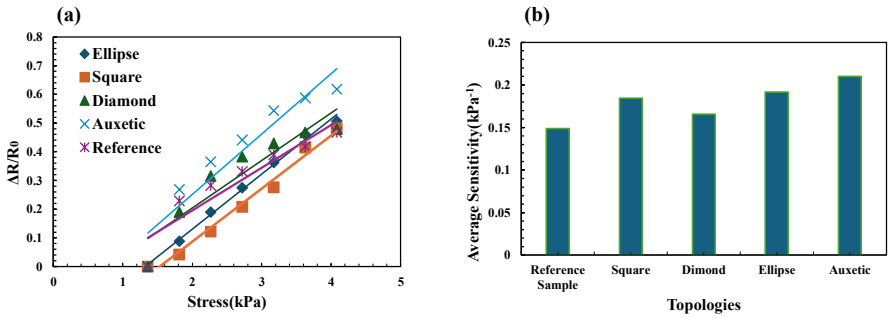

Figure 12. (**a**) Highly sensitive region, (**b**) average sensitivity at highly sensitive region.

The sensitivity was nonlinear in both sensitive regions. The average sensitivity for the lower sensitive region is shown in Figure 13. The formation of a conductive network between nanoparticles significantly influences the material's resistance change. When the piezoresistive material undergoes stress, the formation of the conductive network among nanoparticles may change in a nonlinear manner [57]. A small change in the topology can lead to significant alterations in the formation of the conductive network at lower stress levels, resulting in a rapid decrease in resistance [58]. In addition, as the topology has a significant impact on stress distribution, it can contribute to nonlinear resistance changes at different stress levels [59].

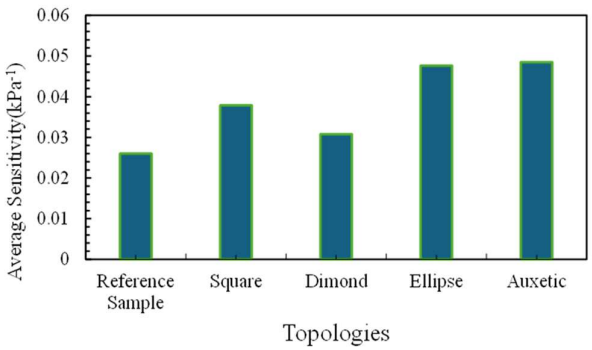

Figure 13. Average sensitivity at lower sensitive region.

5.2.2. Finite Element Analysis Results

Since all samples were made from the same batch of nanocomposite resin, their mechanical and electrical properties were consistent across all topologies. Any variations in electrical properties are attributed to the different topological designs.

An empirical resistivity–stress model was developed to simulate the behavior of the nanocomposite sensor in FEA. A power-law equation was fitted to the highly sensitive region (first portion) of the curve shown in Figure 14, while a third-order polynomial equation was fitted to the less sensitive region (second portion).

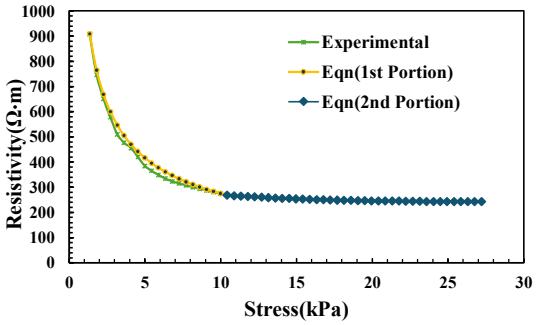

Figure 14. Resistivity vs. stress curve fitting.

The power equation effectively captured the behavior in the higher sensitivity region. This equation is represented as $\rho = 17.442 \cdot {\sigma_1}^{-0.599}$, where $R^2 = 0.9854$, 'ρ' denotes resistivity, and 'σ_1' denotes stress along the compression direction, as illustrated in Figure 15 (left).

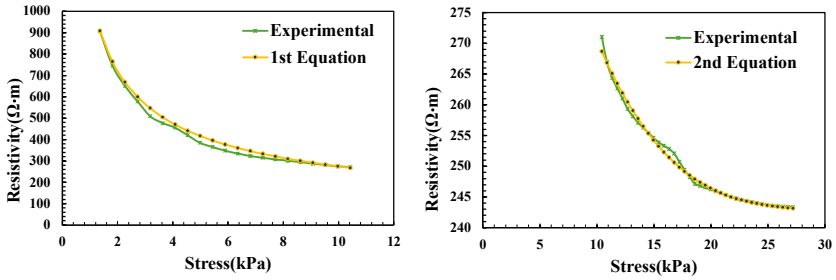

Figure 15. First equation fitting (**Left**), second equation fitting (**Right**).

A third-order polynomial equation was fitted for the lower sensitivity region. This equation is expressed as $\rho = -4{,}600{,}000 \cdot {\sigma_1}^3 + 377{,}000 \cdot {\sigma_1}^2 - 10{,}500 \cdot \sigma_1 + 342.39$, where $R^2 = 0.9917$, as shown in Figure 15 (right).

The polynomial equation provided a more detailed fit for the data in this region, capturing the subtle changes in resistivity under stress.

Figure 16a shows the results of the FEA results for the $\Delta R/R_0$ vs. stress curve across all topologies. The sensitive region in the FEA results reflects the variation in sensitivity among the different topologies. However, unlike the experimental study, the lower sensitive region in the FEA results did not show a distinguishable order of sensitivity. In the lower sensitive region, the variation in stress was not significant enough (Figure 16b) to create distinguishable differences in the plots for the different topologies. Consequently, the FEA simulations did not demonstrate a clear differentiation in sensitivity in this range, which reflected the inherent limitations of the model in capturing the nuanced behavior observed in experimental setups.

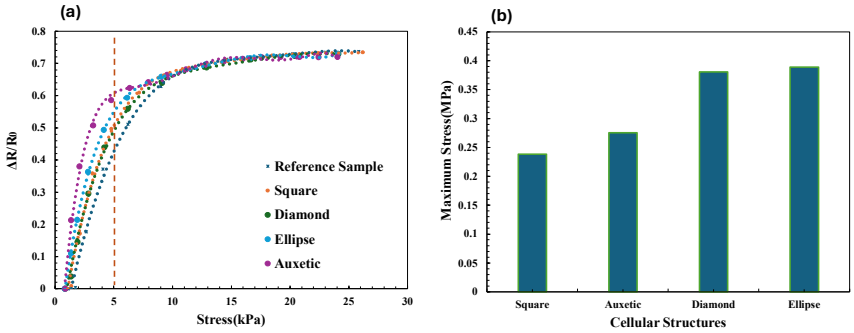

Figure 16. (**a**) $\Delta R/R_0$ vs. stress curves for all topologies (FEA), (**b**) maximum stress for cellular structures.

In real-world samples, factors like material inhomogeneity, contact resistance, and environmental factors can all affect resistivity measurements and may not be accurately captured in FEA. Figure 17 (left) highlights the sensitivity for the higher sensitivity region of the topologies. Figure 17 (right) shows the maximum recorded sensitivity of the cellular structures, aligning with results in the sensitive region from the experimental study.

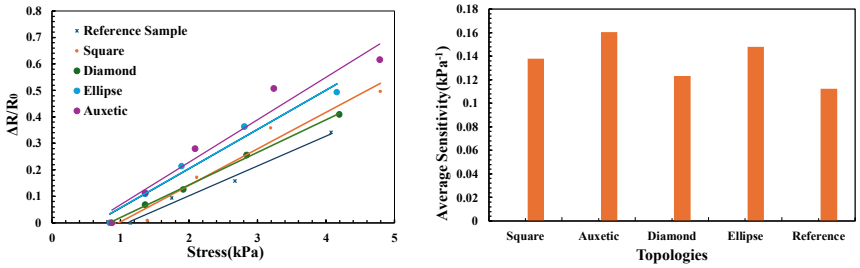

Figure 17. $\Delta R/R_0$ vs. stress curves at high-sensitivity region (**left**), maximum sensitivity for each topology (**right**).

The FEA results closely matched the experimental results in the higher sensitivity region, confirming the accuracy of the FEA model in capturing the fundamental sensitivity trends. However, in the higher stress range, the differences highlighted the complexity of real-world factors that FEA simulations might not fully account for. Despite these variations, the FEA offered valuable insights into the behavior in the higher sensitivity region, reinforcing the experimental findings and providing an additional perspective on the performance of the different topological configurations.

6. Parametric Study

Parametric studies can play a significant role in developing flexible sensors [60] by analyzing how specific geometric parameters influence the sensitivity and flexibility of the sensors. This approach helps to determine which configurations provide the best performance by systematically changing the design parameters of cellular structures. In this study, we selected the ellipse and diamond structure for a parametric study to explore the effects of varying its parameters while maintaining the mass constant across all designs.

Firstly, six different ellipse structures were designed (Figure S3), each with unique aspect ratios of the semi-major axis 'a' and the semi-minor axis 'b' (Table 3).

Table 3. Ellipse structure with varying parameters.

Ellipse Structure	Parameters
ES01	a = 1.5b
ES02	a = 2b
ES03	a = 2.5b
ES04	2.5a = b
ES05	1.5a = b
ES06	a = b

The study aimed to determine how changes in the ellipse's geometry with varying ratios of a to b influence its piezoresistive sensitivity. Maintaining consistent mass across all designs ensured that any observed changes in sensitivity were solely due to geometric variations.

The stress–strain graph (Figure 18a) for the six ellipse structures demonstrates distinct differences in their mechanical behavior. The curve for ES03 was notably different with the lowest stiffness. ES01 shows moderate stiffness while ES04 has the highest stiffness. Figure 18b illustrates the $\Delta R/R_0$ vs. stress curves for each topology, extending up to around 40 kPa and highlighting the most sensitive region up to 7 kPa in Figure 18c. This higher sensitivity region was critical, as it demonstrated the material's response to lower stress levels where significant changes in resistance occurred. The order of piezoresistive sensitivity followed the opposite order of stiffness, with ES03 showing the highest sensitivity, followed by ES02, ES01, ES05, ES06, and ES04 (Figure 18d).

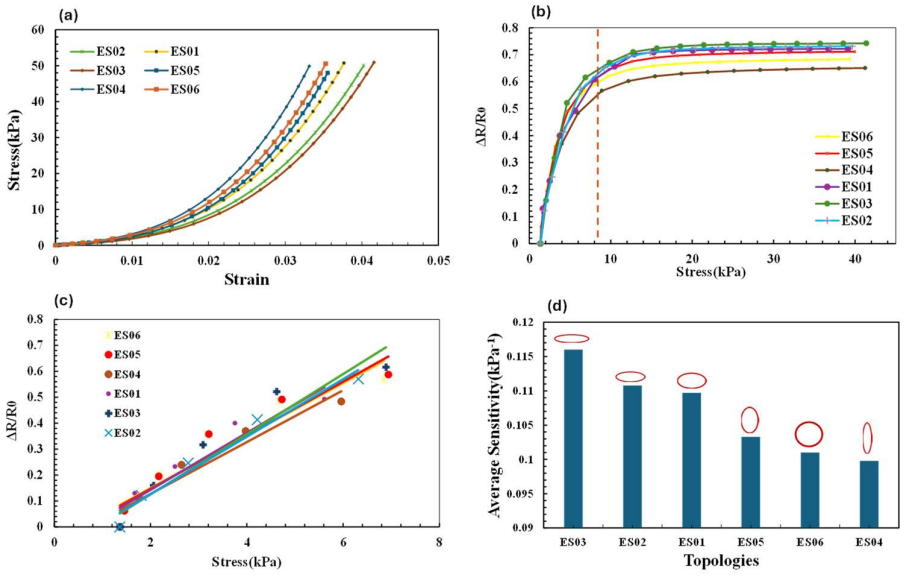

Figure 18. (**a**) Stress vs. strain curves for different ellipse structures. (**b**) $\Delta R/R_0$ vs. stress curves for all ellipse structures, (**c**) $\Delta R/R_0$ vs. stress curves at highly sensitive regions, (**d**) the average sensitivities of the topologies in the higher sensitivity region.

This order highlighted the impact of the semi-major axis length (a) on sensitivity. As the ratio of (a) to (b) increased, the piezoresistive sensitivity also increased. Specifically, ES03, with the largest value of semi-major axis (a) relative to (b), exhibited the highest sensitivity, while ES04, with the smallest ratio, showed the lowest sensitivity.

The hierarchy of stiffness from lowest to highest was ES03, ES02, ES01, ES05, ES06, and ES04. This order demonstrated how changes in the aspect ratios of the ellipse structures impacted their mechanical and piezoresistive performance. In materials with lower stiffness, stress tends to localize in specific regions, leading to concentrated areas of mechanical deformation. This localization enhances the piezoresistive response, as changes in electrical resistance are more pronounced where stress is concentrated. Structures like ES03, which

exhibited the lowest stiffness, also showed the highest piezoresistive sensitivity due to these localized stress areas (Figure S5). This correlation suggested that by optimizing structural design to enhance stress concentration in targeted zones, the sensor's sensitivity can be improved significantly.

To further validate the findings from the ellipse structure, we designed five different diamond structures (Figure S4) with different diagonal lengths ('p' and 'q') (Table 4) and analyzed them.

Table 4. Diamond structure with varying parameters.

Diamond Structure	Parameters
DS01	p = 3q
DS02	p = 2q
DS03	p = q
DS04	2p = q
DS05	3p = q

These structures exhibited a similar trend in the relationship between stiffness and sensitivity (Figure 19). Specifically, the order of stiffness was DS01 > DS02 > DS03 > DS04 > DS05 (Figure S6), while the order of piezoresistivity followed the reverse trend, which was DS01 < DS02 < DS03 < DS04 < DS05.

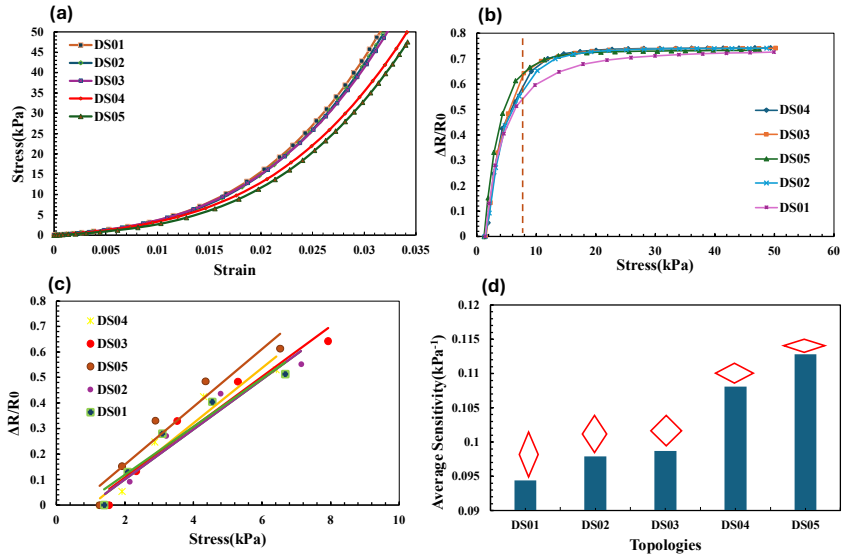

Figure 19. (**a**) Stress vs. strain curves for different diamond structures. (**b**) $\Delta R/R_0$ vs. stress curves, (**c**) $\Delta R/R_0$ vs. stress curves at highly sensitive regions, (**d**) the average sensitivities of the topologies in the higher sensitivity region.

The hierarchy showed a consistent correlation between reduced stiffness and enhanced sensitivity, which we also observed in the ellipse structures. This consistency strengthens the conclusion that geometric parameters significantly influence mechanical behavior and piezoresistive performance.

The parameters of the structures directly impacted how mechanical stress affected electrical resistance. The material's sensitivity can be increased and made to be more responsive to external forces by adjusting these parameters strategically. This parametric study helped us understand how their shape and size affected the sensitivity, which is vital for creating efficient sensor designs.

7. Conclusions

In this paper, we investigated how different topological configurations affected the piezoresistive sensitivity of nanocomposite pressure sensors. We designed four 3D printable cellular structures, namely square, diamond, ellipse, and auxetic, and fabricated those with SLA additive manufacturing techniques. The electromechanical testing showed a comparative analysis of both the mechanical and piezoresistive properties of the topologies. The auxetic structure showed the lowest stiffness and highest sensitivity among the tested configurations. The nonlinear sensitivity was significantly higher in low-stress regions. The hyperelastic Yeoh model demonstrated a better fit for capturing the material's nonlinear behavior in the experimental study and was used as the material model for the FE model. The FE model was validated by the experimental results for the higher sensitivity region from the sensitivity order auxetic > ellipse > square > diamond > reference. FEA provided insights into stress concentration and distribution within the structures. Minor discrepancies in the square and ellipse structures were attributed to imperfections in the 3D-printed samples. Though the material system and void fraction were consistent for all cellular structures, the piezoresistivity varied significantly with the topological designs, highlighting the importance of topological design-centric approaches in tailoring piezoresistive performance.

To further leverage the topological design-centric approach, we conducted a detailed parametric study on the ellipse structure to explore how specific design parameters within the cellular structure affect piezoresistivity. Specifically, the ES03 structure, with the largest aspect ratio, exhibited the highest sensitivity, while the ES04 structure, with the smallest ratio, showed the lowest sensitivity. The stress–strain and resistivity–stress curves indicated that higher aspect ratios led to greater piezoresistive response.

Overall, the research highlighted the importance of topological design-centric approaches in tailoring piezoresistive performance and provided a systematic approach to understanding and optimizing the piezoresistive sensitivity of composite pressure sensors. This approach showed significant promise for developing highly sensitive, customized sensors in areas such as healthcare monitoring and wearable electronics, where precision and adaptability are crucial.

Supplementary Materials: The following supporting information can be downloaded at: https://www.mdpi.com/article/10.3390/applnano5040017/s1, Figure S1: Print bed layout in slicer; Figure S2: Reference cubic sample under uniform pressure; Figure S3: (a) Ellipse parameters. (b) ES01, (c) ES02, (d) ES03, (e) ES04, (f) ES05, (g) ES06; Figure S4: (a) Diamond parameters. (b) DS01, (c) DS02, (d) DS03, (e) DS04, (f) DS05; Figure S5: (a) ES01, (b) ES02, (c) ES03, (d) ES04, (e) ES05, (f) ES06; Figure S6: (a) DS01, (b) DS02, (c) DS03, (d) DS04, (e) DS05.

Author Contributions: Conceptualization, A.E.; Methodology, M.I.K.T.; Software, M.I.K.T.; Validation, M.I.K.T.; Formal Analysis, M.I.K.T. and A.E.; Investigation, A.E. and M.I.K.T.; Resources, M.I.K.T.; Data Curation, M.I.K.T.; Writing—Original Draft Preparation, M.I.K.T.; Writing—Review and Editing, A.E.; Visualization, M.I.K.T.; Supervision, A.E.; Project Administration, A.E. All authors have read and agreed to the published version of the manuscript.

Funding: This research received no external funding.

Data Availability Statement: The raw data supporting the conclusions of this article will be made available by the authors upon request.

Conflicts of Interest: The authors declare no conflicts of interest.

References

1. Gacitua, W.; Ballerini, A.; Zhang, J. Polymer nanocomposites: Synthetic and natural fillers a review. *Maderas Cienc. Tecnol.* **2005**, *7*, 159–178. [CrossRef]
2. Mai, Y.-W.; Yu, Z.-Z. *Polymer Nanocomposites*; Woodhead Publishing: Sawston, UK, 2006.
3. Pozdnyakov, A.; Brzhezinskaya, M.; Vinogradov, A.; Friedrich, K. NEXAFS Spectra of Polymer-nanocarbon Composites. *Fuller. Nanotub. Carbon Nanostruct.* **2008**, *16*, 471–474. [CrossRef]

4. Ahuja, T.; Kumar, D. Recent progress in the development of nano-structured conducting polymers/nanocomposites for sensor applications. *Sens. Actuators B Chem.* **2009**, *136*, 275–286.
5. Yoon, H.; Jang, J. Conducting-polymer nanomaterials for high-performance sensor applications: Issues and challenges. *Adv. Funct. Mater.* **2009**, *19*, 1567–1576. [CrossRef]
6. Yang, J.; Shi, R.; Lou, Z.; Chai, R.; Jiang, K.; Shen, G. Flexible smart noncontact control systems with ultrasensitive humidity sensors. *Small* **2019**, *15*, 1902801. [CrossRef]
7. Carvalho, H.; Tama, D.; Gomes, P.; Abreu, M.; Yao, Y.; Souto, A. Flexible piezoresistive pressure sensors for smart textiles. *IOP Conf. Ser. Mater. Sci. Eng.* **2018**, *459*, 012035. [CrossRef]
8. Guo, Y.; Zhong, M.; Fang, Z.; Wan, P.; Yu, G. A wearable transient pressure sensor made with MXene nanosheets for sensitive broad-range human–machine interfacing. *Nano Lett.* **2019**, *19*, 1143–1150. [CrossRef]
9. Ryu, S.; Lee, P.; Chou, J.B.; Xu, R.; Zhao, R.; Hart, A.J.; Kim, S.-G. Extremely elastic wearable carbon nanotube fiber strain sensor for monitoring of human motion. *ACS Nano* **2015**, *9*, 5929–5936. [CrossRef]
10. Park, J.J.; Hyun, W.J.; Mun, S.C.; Park, Y.T.; Park, O.O. Highly stretchable and wearable graphene strain sensors with controllable sensitivity for human motion monitoring. *ACS Appl. Mater. Interfaces* **2015**, *7*, 6317–6324. [CrossRef]
11. Wang, X.; Gu, Y.; Xiong, Z.; Cui, Z.; Zhang, T. Silk-molded flexible, ultrasensitive, and highly stable electronic skin for monitoring human physiological signals. *Adv. Mater.* **2014**, *26*, 1336–1342. [CrossRef]
12. Lou, Z.; Chen, S.; Wang, L.; Jiang, K.; Shen, G. An ultra-sensitive and rapid response speed graphene pressure sensors for electronic skin and health monitoring. *Nano Energy* **2016**, *23*, 7–14. [CrossRef]
13. Wang, J.-C.; Karmakar, R.S.; Lu, Y.-J.; Chan, S.-H.; Wu, M.-C.; Lin, K.-J.; Chen, C.-K.; Wei, K.-C.; Hsu, Y.-H. Miniaturized flexible piezoresistive pressure sensors: Poly (3, 4-ethylenedioxythiophene): Poly (styrenesulfonate) copolymers blended with graphene oxide for biomedical applications. *ACS Appl. Mater. Interfaces* **2019**, *11*, 34305–34315. [CrossRef] [PubMed]
14. Sang, Z.; Ke, K.; Manas-Zloczower, I. Design strategy for porous composites aimed at pressure sensor application. *Small* **2019**, *15*, 1903487. [CrossRef] [PubMed]
15. Zazoum, B.; Batoo, K.M.; Khan, M.A.A. Recent advances in flexible sensors and their applications. *Sensors* **2022**, *22*, 4653. [CrossRef] [PubMed]
16. Shi, J.; Wang, L.; Dai, Z.; Zhao, L.; Du, M.; Li, H.; Fang, Y. Multiscale hierarchical design of a flexible piezoresistive pressure sensor with high sensitivity and wide linearity range. *Small* **2018**, *14*, 1800819. [CrossRef]
17. Xu, H.; Xie, Y.; Zhu, E.; Liu, Y.; Shi, Z.; Xiong, C.; Yang, Q. Supertough and ultrasensitive flexible electronic skin based on nanocellulose/sulfonated carbon nanotube hydrogel films. *J. Mater. Chem. A* **2020**, *8*, 6311–6318. [CrossRef]
18. Gupta, N.; Adepu, V.; Tathacharya, M.; Siraj, S.; Pal, S.; Sahatiya, P.; Kuila, B.K. Piezoresistive pressure sensor based on conjugated polymer framework for pedometer and smart tactile glove applications. *Sens. Actuators A Phys.* **2023**, *350*, 114139. [CrossRef]
19. Su, F.-C.; Huang, H.-X. Flexible Switching Pressure Sensors with Fast Response and Less Bending-Sensitive Performance Applied to Pain-Perception-Mimetic Gloves. *ACS Appl. Mater. Interfaces* **2023**, *15*, 56328–56336. [CrossRef]
20. Roh, E.; Hwang, B.-U.; Kim, D.; Kim, B.-Y.; Lee, N.-E. Stretchable, transparent, ultrasensitive, and patchable strain sensor for human–machine interfaces comprising a nanohybrid of carbon nanotubes and conductive elastomers. *ACS Nano* **2015**, *9*, 6252–6261. [CrossRef]
21. Wang, X.; Yue, O.; Liu, X.; Hou, M.; Zheng, M. A novel bio-inspired multi-functional collagen aggregate based flexible sensor with multi-layer and internal 3D network structure. *Chem. Eng. J.* **2020**, *392*, 123672. [CrossRef]
22. Zhang, Y.-Z.; Lee, K.H.; Anjum, D.H.; Sougrat, R.; Jiang, Q.; Kim, H.; Alshareef, H.N. MXenes stretch hydrogel sensor performance to new limits. *Sci. Adv.* **2018**, *4*, eaat0098. [CrossRef] [PubMed]
23. Wu, S.; Ladani, R.B.; Zhang, J.; Ghorbani, K.; Zhang, X.; Mouritz, A.P.; Kinloch, A.J.; Wang, C.H. Strain sensors with adjustable sensitivity by tailoring the microstructure of graphene aerogel/PDMS nanocomposites. *ACS Appl. Mater. Interfaces* **2016**, *8*, 24853–24861. [CrossRef] [PubMed]
24. Mohammad Haniff, M.A.S.; Muhammad Hafiz, S.; Wahid, K.A.A.; Endut, Z.; Wah Lee, H.; Bien, D.C.; Abdul Azid, I.; Abdullah, M.Z.; Ming Huang, N.; Abdul Rahman, S. Piezoresistive effects in controllable defective HFTCVD graphene-based flexible pressure sensor. *Sci. Rep.* **2015**, *5*, 14751. [CrossRef] [PubMed]
25. Amjadi, M.; Kyung, K.U.; Park, I.; Sitti, M. Stretchable, skin-mountable, and wearable strain sensors and their potential applications: A review. *Adv. Funct. Mater.* **2016**, *26*, 1678–1698. [CrossRef]
26. Yao, S.; Zhu, Y. Nanomaterial-enabled stretchable conductors: Strategies, materials and devices. *Adv. Mater.* **2015**, *27*, 1480–1511. [CrossRef]
27. Wang, L.; Chiang, W.-H.; Loh, K.J. Topological design of strain sensing nanocomposites. *Sci. Rep.* **2022**, *12*, 9179. [CrossRef] [PubMed]
28. Lin, Y.A.; Zhao, Y.; Wang, L.; Park, Y.; Yeh, Y.J.; Chiang, W.H.; Loh, K.J. Graphene K-Tape meshes for densely distributed human motion monitoring. *Adv. Mater. Technol.* **2021**, *6*, 2000861. [CrossRef]
29. Kim, E.; Khaleghian, S.; Emami, A. Behavior of 3D printed stretchable structured sensors. *Electronics* **2022**, *12*, 18. [CrossRef]
30. Banks, J.D.; Khaleghian, M.; Emami, A. Effects of Infill on the Additive Manufacturing of Piezoresistive Pressure Sensors. In Proceedings of the ASME 2022 International Mechanical Engineering Congress and Exposition, Columbus, OH, USA, 30 October–3 November 2022.

31. Bhate, D. Classification of Cellular Solids. Available online: https://www.padtinc.com/2016/08/29/classification-of-cellular-solids-and-why-it-matters/ (accessed on 11 April 2024).
32. Pilkey, W.D.; Pilkey, D.F.; Bi, Z. *Peterson's Stress Concentration Factors*; John Wiley & Sons: Hoboken, NJ, USA, 2020.
33. Costa, J.C.; Spina, F.; Lugoda, P.; Garcia-Garcia, L.; Roggen, D.; Münzenrieder, N. Flexible sensors—From materials to applications. *Technologies* **2019**, *7*, 35. [CrossRef]
34. Ahn, K.; Kim, K.; Kim, J. Thermal conductivity and electric properties of epoxy composites filled with TiO_2-coated copper nanowire. *Polymer* **2015**, *76*, 313–320. [CrossRef]
35. Gong, S.; Zhao, Y.; Yap, L.W.; Shi, Q.; Wang, Y.; Bay, J.A.P.; Lai, D.T.; Uddin, H.; Cheng, W. Fabrication of highly transparent and flexible nanomesh electrode via self-assembly of ultrathin gold nanowires. *Adv. Electron. Mater.* **2016**, *2*, 1600121. [CrossRef]
36. Dickey, M.D.; Chiechi, R.C.; Larsen, R.J.; Weiss, E.A.; Weitz, D.A.; Whitesides, G.M. Eutectic gallium-indium (EGaIn): A liquid metal alloy for the formation of stable structures in microchannels at room temperature. *Adv. Funct. Mater.* **2008**, *18*, 1097–1104. [CrossRef]
37. Jiang, J.; Li, Y.; Liu, J.; Huang, X.; Yuan, C.; Lou, X.W. Recent advances in metal oxide-based electrode architecture design for electrochemical energy storage. *Adv. Mater.* **2012**, *24*, 5166–5180. [CrossRef] [PubMed]
38. Lee, T.; Lee, W.; Kim, S.W.; Kim, J.J.; Kim, B.S. Flexible textile strain wireless sensor functionalized with hybrid carbon nanomaterials supported ZnO nanowires with controlled aspect ratio. *Adv. Funct. Mater.* **2016**, *26*, 6206–6214. [CrossRef]
39. Huang, J.C. Carbon black filled conducting polymers and polymer blends. *Adv. Polym. Technol. J. Polym. Process. Inst.* **2002**, *21*, 299–313. [CrossRef]
40. Abshirini, M.; Charara, M.; Liu, Y.; Saha, M.; Altan, M.C. 3D printing of highly stretchable strain sensors based on carbon nanotube nanocomposites. *Adv. Eng. Mater.* **2018**, *20*, 1800425. [CrossRef]
41. Secor, E.B.; Prabhumirashi, P.L.; Puntambekar, K.; Geier, M.L.; Hersam, M.C. Inkjet printing of high conductivity, flexible graphene patterns. *J. Phys. Chem. Lett.* **2013**, *4*, 1347–1351. [CrossRef]
42. Bonavolontà, C.; Camerlingo, C.; Carotenuto, G.; De Nicola, S.; Longo, A.; Meola, C.; Boccardi, S.; Palomba, M.; Pepe, G.P.; Valentino, M. Characterization of piezoresistive properties of graphene-supported polymer coating for strain sensor applications. *Sens. Actuators A Phys.* **2016**, *252*, 26–34. [CrossRef]
43. NextGen 3Dresyn TFA70 Tough & Foldable with SHORE A70. Available online: https://www.3dresyns.com/products/nextgen-3dresyn-tfa70-tough-foldable-with-shore-a70 (accessed on 21 March 2024).
44. 3D-ADD GrapEK1 Bio, Biocompatible Electrically Conductive Nano Graphene 3D Additive. Available online: https://www.3dresyns.com/products/3d-add-grapek1-bio-biocompatible-electrically-conductive-nano-graphene-3d-additive?_pos=2&_sid=9ed40c20f&_ss=r (accessed on 21 March 2024).
45. Khatibi, E. Piezoresistivity of Graphene. 2010. Available online: https://www.politesi.polimi.it/handle/10589/16787 (accessed on 13 May 2024).
46. Banks, J.D.; Emami, A. Carbon-based piezoresistive polymer nanocomposites by extrusion additive manufacturing: Process, material design, and current progress. *3D Print. Addit. Manuf.* **2024**, *11*, e548–e571. [CrossRef]
47. Smith, A.D.; Niklaus, F.; Paussa, A.; Schröder, S.; Fischer, A.C.; Sterner, M.; Wagner, S.; Vaziri, S.; Forsberg, F.; Esseni, D. Piezoresistive properties of suspended graphene membranes under uniaxial and biaxial strain in nanoelectromechanical pressure sensors. *ACS Nano* **2016**, *10*, 9879–9886. [CrossRef]
48. Al Zoubi, N.F.; Tarlochan, F.; Mehboob, H. Mechanical and fatigue behavior of cellular structure Ti-6AL-4V alloy femoral stems: A finite element analysis. *Appl. Sci.* **2022**, *12*, 4197. [CrossRef]
49. Liu, F.; Zhang, D.Z.; Zhang, P.; Zhao, M.; Jafar, S. Mechanical properties of optimized diamond lattice structure for bone scaffolds fabricated via selective laser melting. *Materials* **2018**, *11*, 374. [CrossRef] [PubMed]
50. Dos Reis, F.; Ganghoffer, J. Equivalent mechanical properties of auxetic lattices from discrete homogenization. *Comput. Mater. Sci.* **2012**, *51*, 314–321. [CrossRef]
51. Chung, J.Y.; Chastek, T.Q.; Fasolka, M.J.; Ro, H.W.; Stafford, C.M. Quantifying residual stress in nanoscale thin polymer films via surface wrinkling. *Acs Nano* **2009**, *3*, 844–852. [CrossRef] [PubMed]
52. Kishore, V.; Chen, X.; Hassen, A.; Lindahl, J.; Kunc, V.; Duty, C. *Effect of Post-Processing Annealing on Crystallinity Development and Mechanical Properties of Polyphenylene Sulfide Composites Printed on Large-Format Extrusion Deposition System*; Oak Ridge National Laboratory (ORNL): Oak Ridge, TN, USA, 2019.
53. Thi, T.B.N.; Ata, S.; Morimoto, T.; Kato, Y.; Horibe, M.; Yamada, T.; Okazaki, T.; Hata, K. Annealing-induced enhancement of electrical conductivity and electromagnetic interference shielding in injection-molded CNT polymer composites. *Polymer* **2022**, *245*, 124680.
54. Seok, W.; Jeon, E.; Kim, Y. Effects of annealing for strength enhancement of FDM 3D-printed ABS reinforced with recycled carbon fiber. *Polymers* **2023**, *15*, 3110. [CrossRef]
55. Mooney-Rivlin Model. Available online: https://www.sciencedirect.com/topics/engineering/mooney-rivlin-model (accessed on 11 April 2024).
56. Hyperelastic Model Comparison. Available online: https://reference.wolfram.com/language/PDEModels/tutorial/StructuralMechanics/ModelCollection/HyperelasticModelComparison.html (accessed on 28 May 2024).
57. Zang, Y.; Zhang, F.; Di, C.-A.; Zhu, D. Advances of flexible pressure sensors toward artificial intelligence and health care applications. *Mater. Horiz.* **2015**, *2*, 140–156. [CrossRef]

58. Nurprasetio, I.P.; Budiman, B.A.; Afwan, A.A.; Halimah, P.N.; Utami, S.T.; Aziz, M. Nonlinear piezoresistive behavior of plain-woven carbon fiber reinforced polymer composite subjected to tensile loading. *Appl. Sci.* **2020**, *10*, 1366. [CrossRef]
59. Azam, M.U.; Schiffer, A.; Kumar, S. Mechanical and piezoresistive properties of GNP/UHMWPE composites and their cellular structures manufactured via selective laser sintering. *J. Mater. Res. Technol.* **2024**, *28*, 1359–1369. [CrossRef]
60. Devi, R.; Gill, S.S.; Singh, B. Parametric evaluation of carbon nano-tube based piezoresistive pressure sensor. *Mater. Today Proc.* **2022**, *71*, 357–361. [CrossRef]